An Efficient Numerical Contour Deformation Method for Calculating Electromagnetic Scattered Fields from 3-D Convex Scatterers

Yu Mao Wu[1], Weng Cho Chew[2, *], Ya-Qiu Jin[1], Tie Jun Cui[3], and Li Jun Jiang[4]

Abstract—We consider the accuracy improvement of the high frequency scattered fields from 3-D convex scatterers. The Fock currents from the convex scatterers are carefully studied. Furthermore, we propose the numerical contour deformation method to calculate the Fock currents with frequency independent workload and error controllable accuracy. Then, by adopting the Fock currents and the incremental length diffraction coefficient (ILDC) technique, the scattered fields are clearly formulated. Compared to physical optics (PO) scattered fields from 3-D convex sphere, numerical results demonstrate significant accuracy enhancement of the scattered field via the Fock current approach.

1. INTRODUCTION

In computational electromagnetics (CEM) community, the efficient algorithm for calculating the scattered field from electrically large scatterer remains as an important and challenging problem [1]. With respect to the wave physics, the high frequency scattered fields from the electrically large convex scatterers follow the ray physics. For the electromagnetic wave impinging on the convex scatterer, the surface diffracted ray fields occur at the shadow boundary lines of the curved surfaces. Then, at the grazing incident angles, the diffracted ray fields may appear at the shadow boundary lines over the convex surfaces. In the shadow region, due to the diffraction rays at the shadow boundary lines, the creeping ray fields occur. Furthermore, for the calculation of the scattered fields, the creeping wave fields have the non-ignorable contributions [3–7, 11, 12, 17].

The high frequency methods could be classified as the current based methods and ray field based methods. With the aid of the ray physics theory, the geometrical ray-tracing technique method was developed, like the shooting and bouncing ray method (SBR) [2]. The typical current based method is the PO method. However, due to the inaccurate approximation of the PO current around the transition region and in the shadow region of the scatterer, the scattered fields loose accuracy with the observation point located in these regions. To improve the accuracy of the scattered field, researchers proposed the incremental diffraction techniques, for instance, the physical theory of diffraction (PTD), the ILDC [6, 7, 10–14] and the incremental theory of diffraction (ITD) [3–5]. Based on the incremental theory of diffraction localization process for the canonical problems, the incremental field contributions are presented by a general procedure in [3]. The fringe incremental diffraction techniques may improve the accuracy of the PO scattered problems from the perfectly conducting canonical wedge. The ILDC technique corresponds to the differential field generated by the linear radiation integral of non-uniform strips current, for instance, the Fock and Fringe currents for the convex and wedge scatterers [3, 6, 13], respectively. The incremental length diffraction fields are deduced from the local canonical problems

[1] Key Laboratory for Information Science of Electromagnetic Waves, School of Information Science and Technology, Fudan University, Shanghai 200433, China. [2] Department of Electrical and Computer Engineering, University of Illinois at Urbana-Champaign (on part-time appointment with HKU) Urbana, IL 61801, USA. [3] State Key Laboratory of Millimeter Waves, Southeast University, Nanjing 210096, China. [4] Department of Electric and Electronic Engineering, The University of Hong Kong Pokfulam Road, Hong Kong SAR, China.

with the 2-D uniform cylindrical configuration by the ILDC technique. In particular, when the difference between the exact current and the PO current (named as the non-uniform (NU) current) is well approximated, the accuracy of the PO scattered field could be significantly improved by the ILDC technique. Hence, the ILDC technique offers an efficient way to enhance the accuracy of scattered fields from the 3-D convex scatterer.

Compared to the work in [21], the three main advances in this work are, first, the hybridization of the numerical contour deformation method and the high frequency asymptotic method was developed to calculate the Fock current efficiently. In this situation, the computational effort for the Fock current could be achieved in the frequency independent manner. Second, the ILDC technique together with the numerical contour deformation method was adopted to fast calculate the scattered fields from the 3-D convex sphere. Third, the Fock current from the 3-D convex sphere in the spherical coordinate system was clearly given. The high frequency wave physics from the convex scatterer, including the creeping wave fields, the shadow boundary, and the Fock current are clearly captured by the numerical contour deformation method. The paper is organized as follows. In Section 2, we introduce the ILDC formulation. In Section 3, the Fock current from the PEC sphere is carefully studied. In Section 4, the high frequency scattered fields are clearly given via the Fock current. Sections 5–6 present the efficient numerical contour deformation technique to evaluate the Fock current, and the numerical results of the scattered fields from the convex perfect electric conductor sphere. We make the conclusion in Section 7.

2. ILDC TECHNIQUE FOR THE 3-D CONVEX SCATTERERS

2.1. ILDC Technique for the Convex Cylinder

To elegantly present the ILDC technique, we start with the 3-D convex cylinder as shown in Figure 1. We assume that the integration surface from the cylinder is expressed by $S(x, y, z)$. Furthermore, the projection of $S(x, y, z)$ on the x-y plane is denoted as $C(x, y)$, that is, the cross section of the 3-D convex cylinder. Along the z-axis, the 3-D convex cylinder is bounded by an finite integration domain $[z_a, z_b]$. By performing the integration of the free space dyadic Green's function and the uniform Fock current
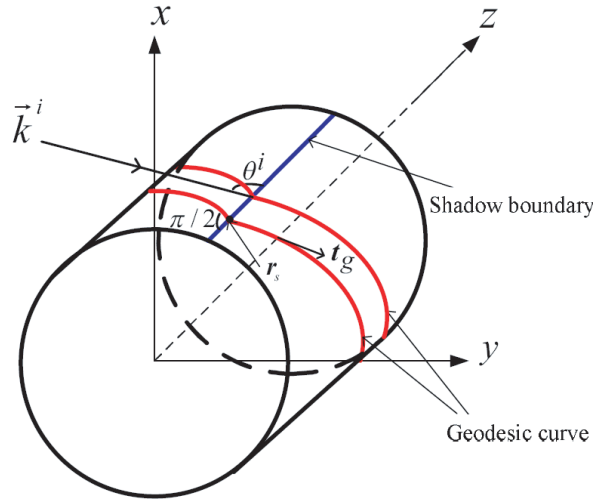
Figure 1. The obliquely incident plane wave with wavevector $\mathbf{k}^i$ impinges on the convex cylinder with finite length, the shadow boundary is shown by the blue line on the cylinder. The Fock current on the shadow region follows the direction of the geodesic curve $C(z, s)$ by the magenta color. In the shadow region, the tangential direction of $C(z, s)$ is denoted by $\hat{\mathbf{t}}_g$, which forms a constant angle $\pi - \theta^i$ with z axis. In the lit region, $\hat{\mathbf{t}}_g$ forms $\pi/2$ with z axis.

over $S(x, y, z)$, we have

$$\mathbf{E}^{(s,q)}(\mathbf{r}) = i\omega\mu \left(\mathbf{I} + \frac{\nabla\nabla}{k^2}\right) \cdot \int_S d\mathbf{r}' \frac{\mathbf{K}^{(q)}(\hat{\mathbf{r}}^i, \mathbf{r}')e^{ik|\mathbf{r}-\mathbf{r}'|}}{4\pi|\mathbf{r}-\mathbf{r}'|} \tag{1}$$

Here, $\hat{\mathbf{r}}^i$ is the unit vector of the incident wave vector $\mathbf{r}^i$, and $\mathbf{r}'$ is the integration source points. $\mathbf{K}^{(q)}(\hat{\mathbf{r}}^i, \mathbf{r}')$ represents the uniform Fock current, which will be comprehensively studied in Section 3. The index q denotes the TE and TM cases. For notation convenience, we omit the index q in the rest of this paper. In the far field, Equation (1) could be formulated as

$$\mathbf{E}^{(s)}(\mathbf{r}) \approx \frac{ike^{ikr}}{4\pi r} Z \left(\hat{\theta}\hat{\theta} + \hat{\phi}\hat{\phi}\right) \cdot \int_S d\mathbf{r}' e^{-ik\hat{\mathbf{r}}\cdot\mathbf{r}'} \mathbf{K}\left(\hat{\mathbf{r}}^i, \mathbf{r}'\right) \tag{2}$$

Here, $Z = \sqrt{\frac{\mu}{\epsilon}}$. $\hat{\theta}$ and $\hat{\phi}$ are the directions along θ- and ϕ- axes in the spherical coordinate system $\{r, \theta, \phi\}$. To adopt the ILDC technique, we consider the differential formulation of $S(x, y, z)$ with respect to the z-axis, which is given by $dS(x, y, z) = \widetilde{C}(s) \times dz$. Here, $\widetilde{C}(s)$ is the parameterization of contour $C(x, y)$ on the x-y plane with the parameter s. In the illuminated region, $\widetilde{C}(s)$ is normal to the shadow boundary, that is, $\widetilde{C}(s)$ follows the direction of the incident wavevector $\hat{\mathbf{k}}^i$. In the shadow region, $\widetilde{C}(s)$ is the geodesic curve whose tangential direction forms θ^i angle with the z-axis, as shown in Figure 1. Then, the scattered fields $d\mathbf{E}^{(s)}(\mathbf{r})$ at the observation point $\mathbf{r}$ away from the incremental current sheet of length dz could be formulated as

$$d\mathbf{E}^{(s)}(\mathbf{r}) \approx dz \frac{ike^{ikr}Z}{4\pi r} \left(\hat{\theta}\hat{\theta} + \hat{\phi}\hat{\phi}\right) \cdot \int_{\widetilde{C}(s)} d\mathbf{r}' e^{-ik\hat{\mathbf{r}}\cdot\mathbf{r}'} \mathbf{K}(\hat{\mathbf{r}}^i, \mathbf{r}') \tag{3}$$

The shadow boundary curve is governed by

$$\hat{\mathbf{r}}^i \cdot \hat{\mathbf{n}}_s(\mathbf{r}_s) = 0 \tag{4}$$

Where $\hat{\mathbf{n}}_s(\mathbf{r}_s)$ is the outward unit normal vector from the point $\mathbf{r}_s$ lying on shadow boundary of the convex cylinder. On invoking the ILDC technique, we could see that Equation (3) represents the incremental length scattered fields along z direction. The scattering problem from 3-D cylinder is approximated as the summation of 2-D cylinder scattering problems in the ILDC approach. Moreover, we could see that the Fock current in Equation (3) could be derived from a 2-D canonical cylinder scattering problem [9, 16].

By subtracting the PO current from the Fock current, we have the non-uniform (NU) incremental diffraction wave fields around the transition region of the scatterer as

$$d\mathbf{E}^{(s,NU)}(\mathbf{r}) \approx dz \frac{ike^{ikr}}{4\pi r} Z \left(\hat{\theta}\hat{\theta} + \hat{\phi}\hat{\phi}\right) \cdot \int_{\widetilde{C}(s)} d\mathbf{r}' e^{-ik\hat{\mathbf{r}}\cdot\mathbf{r}'} \mathbf{K}^{(NU)}(\hat{\mathbf{r}}^i, \mathbf{r}') \tag{5}$$

Here,

$$\mathbf{K}(\hat{\mathbf{r}}^i, \mathbf{r}') = \mathbf{K}^{(PO)}(\hat{\mathbf{r}}^i, \mathbf{r}') + \mathbf{K}^{(NU)}(\hat{\mathbf{r}}^i, \mathbf{r}') \tag{6}$$

The term $\mathbf{K}^{(PO)}(\hat{\mathbf{r}}^i, \mathbf{r}')$ corresponds to the PO current in the scatterer's lit region, and $\mathbf{K}^{(NU)}(\hat{\mathbf{r}}^i, \mathbf{r}')$ is the NU-Fock current near the transition region and in the deep shadow region. Equation (5) expresses the incremental field radiated by a strip of thickness dz from the convex cylinder surface with the cross section curve $\widetilde{C}(s)$. The computations of the Fock current in Equation (3) or NU-Fock current in Equation (5) with large parameters will occur when the observation point $\mathbf{r}$ lies far away from the shadow boundaries of the convex scatterer.

2.2. ILDC Technique for the Convex Sphere

Next, we consider the 3-D convex sphere as shown in Figure 2(a). In order to adopt the ILDC technique for the sphere, first, we denote that $\mathbf{r}'$ forms the angle ϕ_1 with the x_0-axis, and the projection vector in the x_0-y_0 plane is denoted as $\rho_{xy}(\phi_1)$. Next, when we cut the 3-D convex sphere in the $\hat{\rho}_{xy}(\phi_1)$-z_0 plane, a 2-D circle $X(\rho_{xy}(\phi_1), \phi_1, z_0)$ with radius R is always formed. Then, by looping ϕ_1 from 0 to 2π for
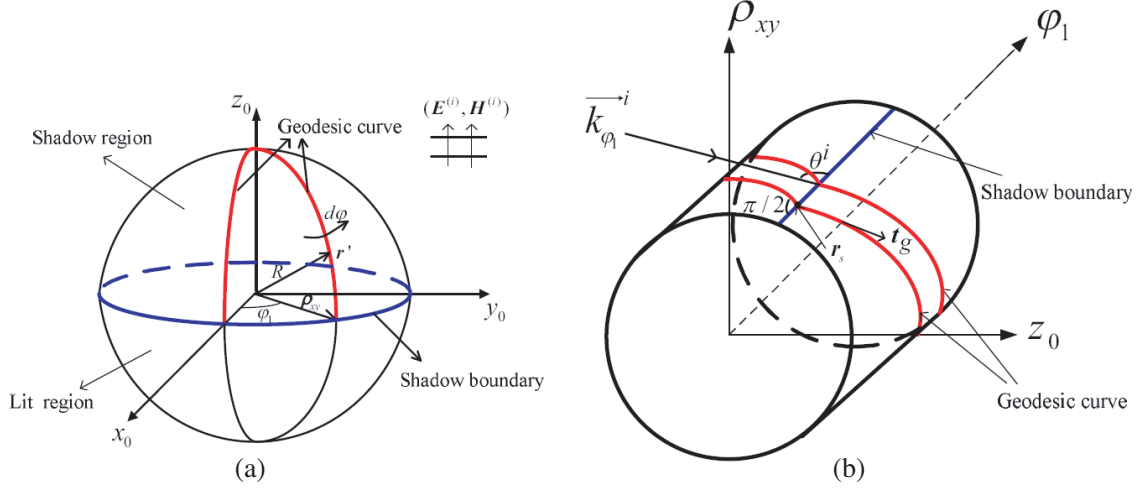
Figure 2. (a) The 3-D electrically large PEC sphere with incident plane wave. The lit and shadow regions are demonstrated in the figure. The lit and shadow regions are separated by the shadow boundary, denoted by the blue line. The Fock current on the shadow region follows the direction of the geodesic curve by the red color. (b) 3-D convex cylinder in the $\{\hat{\rho}_{xy}(\phi_1), z_0, \hat{\phi}_1\}$ coordinate system with the plane wave $\mathbf{k}_{\varphi_1}{}^i$ incident on the cylinder.
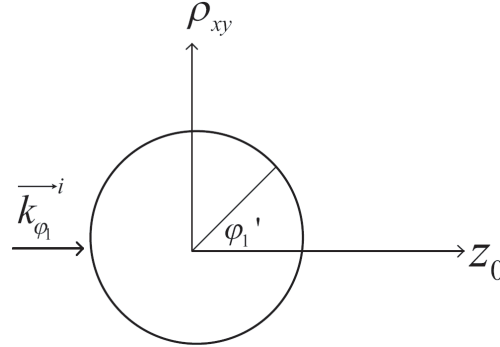
Figure 3. The ILDC technique used for the sphere, geometry of $X(\rho_{xy}(\phi_1), z_0, \phi_1)$ with radius R.

the 2-D circle $X(\rho_{xy}(\phi_1), \phi_1, z_0)$, the 3-D convex sphere is always constructed. In this manner, with the incremental length direction along $\hat{\phi}_1$, the 3-D sphere could be reduced to the summation of cylinders with the cross sections $X(\rho_{xy}(\phi_1), \phi_1, z_0)$ and axes $\hat{\phi}_1$. In Figure 2(b), we demonstrate the geometries of these cylinders. At this point, the ILDC technique introduced in section II could be successfully applied for the 3-D sphere. Then, we assume that the projection of $\mathbf{r}'$ in Equation (5) in the $\hat{\rho}_{xy}(\phi_1)$-z plane forms the angle ϕ_1' with the z-axis, as shown in Figure 3. Furthermore, $X(z, \rho_{xy}(\phi_1), \phi_1)$ could be parameterized as $C(\phi_1, \phi_1')$, as shown in Figure 3. Hence, we could reformulate Equation (5), and then obtain

$$d\mathbf{E}^{(NU)}(\mathbf{r}) \approx d\phi_1 Z \frac{ike^{ikr}}{4\pi r} \left(\hat{\theta}\hat{\theta} + \hat{\phi}\hat{\phi} \right) \cdot \int_{C(\phi_1, \phi_1')} d\phi_1' \mathbf{F}^{(NU)}(\theta^i, \phi^i, \phi_1, \phi_1') \tag{7}$$

Here,

$$\mathbf{F}^{(NU)}(\theta^i, \phi^i, \phi_1, \phi_1') = C_{\phi_1'}'(\phi_1, \phi_1')e^{-ik\hat{\mathbf{r}}\cdot\mathbf{r}'}\mathbf{K}^{(NU)}(\theta^i, \phi^i, \phi_1, \phi_1') \tag{8}$$

And $\mathbf{r}'$ can be further represented as

$$\mathbf{r}' = R[\sin\phi_1' \cos\phi_1, \sin\phi_1' \sin\phi_1, \cos\phi_1']^T$$

which expresses the source points $\mathbf{r}'$ along the curve $C(\phi_1, \phi_1')$.

3. THE FOCK CURRENT EXPRESSIONS

Let an orthogonal system $(\hat{\mathbf{h}}^i, \hat{\mathbf{v}}^i, \hat{\mathbf{k}}^i)$ be defined at the point $\mathbf{r}'$, and

$$\hat{\mathbf{k}}^i = \left[\sin\theta^i\cos\phi^i, \sin\theta^i\sin\phi^i, \cos\theta^i\right]^T \tag{9}$$

with θ^i and ϕ^i denoted as the angles between $\hat{\mathbf{k}}^i$ and the z- and x- axes, respectively. And the unit vectors $\hat{\mathbf{h}}^i$ and $\hat{\mathbf{v}}^i$ are the local polarization directions of $\mathbf{E}^i$ and $\mathbf{H}^i$ at the source point $\mathbf{r}'$. Under the TE-TM decomposition theorem of the plane wave in the homogeneous medium, the plane wave illuminated on the circular cylinder in Figure 2(b) could be decomposed as

$$\mathbf{E}^{(i)} = \left(E_{\theta^i}\hat{\theta}^i + E_{\phi^i}\hat{\phi}^i\right)e^{ik\hat{\mathbf{k}}^i\cdot\mathbf{r}} \tag{10}$$

For the source point $\mathbf{r}'$ lying in the scatterer's lit region, the TE component of the Fock current takes the expression

$$\mathbf{K}^{(TE)}(\mathbf{r}') = \mathbf{K}^{(TE)}(\theta^i, \phi^i, \phi_1, \phi_1') = \hat{\mathbf{n}}(\mathbf{r}') \times \mathbf{H}^{(i,TE)}(\mathbf{r}')G_{TE}\left(\left(\frac{kR}{2}\right)^{\frac{1}{3}}\hat{\mathbf{n}}(\mathbf{r}')\cdot\hat{\mathbf{k}}^i\right) \tag{11}$$

Here, $\hat{\mathbf{n}}(\mathbf{r}')$ is the outward normal vector of the considered scatterer at $\mathbf{r}'$. Where $G_{TE}(x)$ is the Fock function with the formulation

$$G_{TE}(x) = e^{ix^3/3}g(x) \tag{12}$$

$$g(x) = -\frac{e^{i\pi/6}}{2\pi}\int_\Gamma \frac{e^{ixt}}{Ai'(te^{i2\pi/3})}dt \tag{13}$$

The term $Ai(x)$ in Equation (13) expresses the Airy function with the Stokes' phenomenon on the complex plane, and $\Gamma = \Gamma(t)$ is the integration path demonstrated in Figure 4. Furthermore, $\Gamma(t)$ represents the contour on the complex plane that follows the path starting from $-\infty$ in the angular domain $\frac{1}{3\pi} < \arg(t) < \pi$, passing through the origin and ending at ∞ in the angular domain $-\frac{1}{3\pi} < \arg(t) < \frac{1}{3\pi}$. Here, t is a complex path parameter in Figure 5 which could be parameterized as $t = t(s)$, with s as a real parameter.
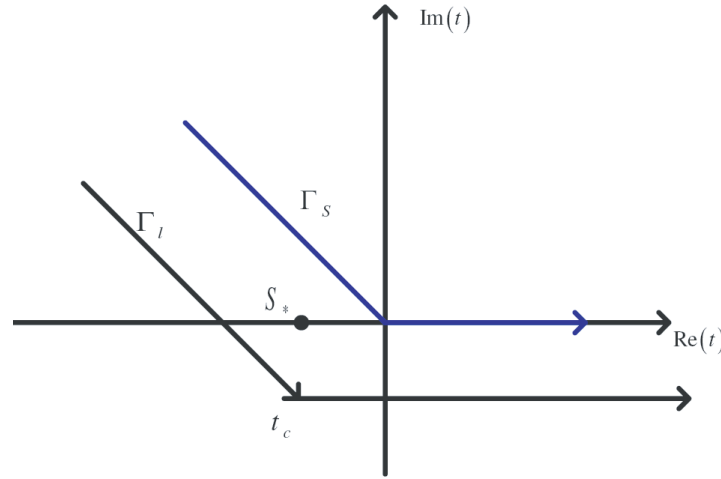
Figure 4. The integration paths Γ_l and Γ_s adopted in the calculation of the Fock function $g(x)$, with the observation point $\mathbf{r}$ lying in the lit and shadow regions of the scatterer, respectively. Here, $S_* = -x^2$ is the saddle point.

After some mathematical derivations [20], the Fock current in Equation (11) could be re-formulated as

$$\mathbf{K}^{(TE)}\left(\theta^i, \phi^i, \phi_1, \phi_1'\right) = Y_0\left(-\cos\phi_1'\hat{\mathbf{x}} + \sin\phi_1'\cos\phi_1\hat{\mathbf{z}}\right)e^{ik\cos\phi_1'}G_{TE}\left(\left(\frac{kR}{2}\right)^{\frac{1}{3}}\cos\phi_1'\right), \quad \phi_1' \in [\pi/2, \pi] \tag{14}$$
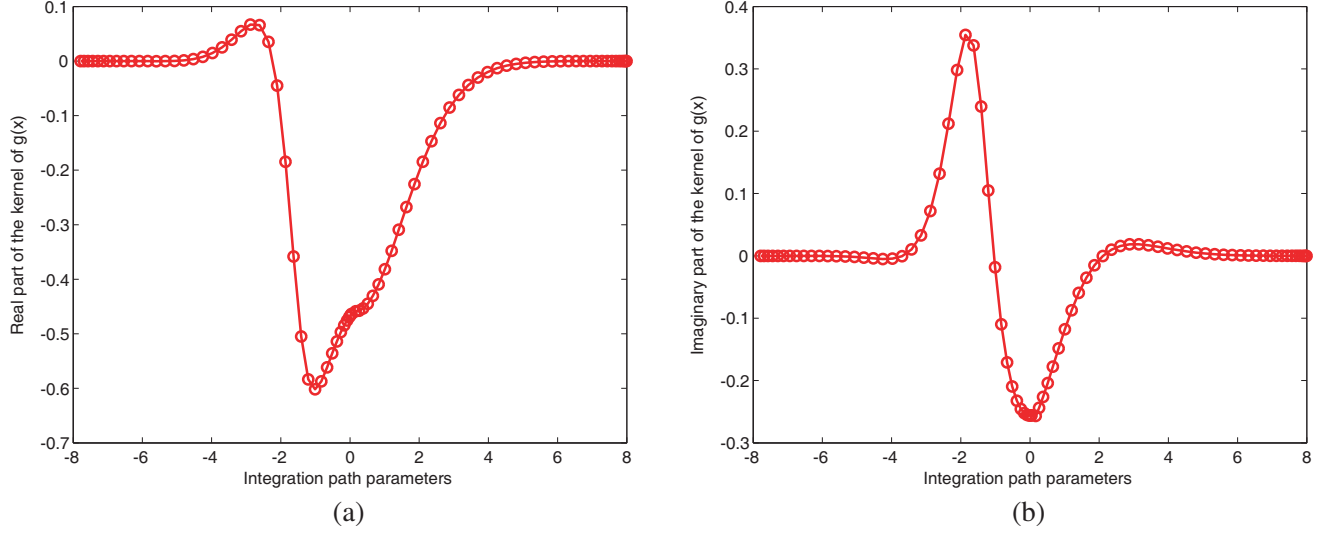
Figure 5. (a), (b) Real and imaginary components of the integrand in the Fock function $g(x)$ after adopting the contour deformation path Γ_l, respectively. Here, the observation point lies in the lit region of the scatterer, and the parameter x takes the value $x = -1.0074$. The abscissas in Figure 5 denote the real s parameter, which could be obtained by the parameterization process $t = t(s)$ along the contour path Γ_l.

Here, we shall note that the parameter $(\frac{kR}{2})^{\frac{1}{3}} \cos \phi'_1$ in Equation (14) is negative with the source point $\mathbf{r}'$ lying in the lit region of the scatterer.

For the source point $\mathbf{r}'$ lying in the shadow region of the scatterer, $\mathbf{K}^{(TE)}(\mathbf{r}')$ takes the expression

$$\mathbf{K}^{(TE)}(\mathbf{r}') = Y_0 \hat{\mathbf{n}}_s(\mathbf{r}_s) \cdot \mathbf{E}^{(i,TE)}(\mathbf{r}_s) e^{iks_g(\mathbf{r}')} g(x_g) \left(\frac{\rho(\mathbf{r}_s)}{\rho_g(\mathbf{r}')} \right)^{\frac{1}{6}} \hat{\mathbf{t}}_g \tag{15}$$

Here, $\mathbf{r}_s$ is the point lying along the shadow boundary. And $\hat{\mathbf{t}}_g$ in Equation (15) is the tangential direction of the geodesic curve as shown in Figure 2(b), which may be torsional. After some math derivations [20], $\mathbf{K}^{(TE)}(\mathbf{r}')$ in Equation (15) could be expressed as

$$\mathbf{K}^{(TE)} \left(\theta^i, \phi^i, \phi_1, \phi'_1 \right) = -\hat{\phi}'_1 \sin \phi'_1 \cos \phi_1 e^{ikR \left| \frac{\pi}{2} - \phi'_1 \right|} g \left(\left(\frac{kR}{2} \right)^{\frac{1}{3}} \left| \frac{\pi}{2} - \phi'_1 \right| \right), \phi'_1 \in \left[0, \frac{\pi}{2} \right] \tag{16}$$

Equation (16) above is the expression of the Fock current in the shadow region of the 3-D convex sphere. Similar argument holds for the TM case. In particular, the TM case Fock function $G_{TM}(x)$ is defined by [13, 20]:

$$G_{TM}(x) = e^{ix^3/3} f(x) \tag{17}$$

$$f(x) = \frac{e^{-i\pi/6}}{2\pi} \int_\Gamma \frac{e^{ixt}}{Ai(te^{i2\pi/3})} dt \tag{18}$$

4. HIGH FREQUENCY SCATTERED FIELDS

After obtaining the Fock current from the 3-D convex sphere, we study the high frequency scattered fields. $\mathbf{E}^{(s)}(\mathbf{r})$ in Equation (2) could be reformulated as

$$\mathbf{E}^{(s)}(\mathbf{r}) = Z \frac{ikR^2 e^{ikr}}{4\pi r} \left(\hat{\theta}\hat{\theta} + \hat{\phi}\hat{\phi} \right) \cdot \int_0^{2\pi} d\phi_1 \int_0^\pi d\phi'_1 \mathbf{F}_1 \left(\theta^i, \phi^i, \phi_1, \phi'_1 \right) \tag{19}$$

Here,

$$\mathbf{F}_1\left(\theta^i, \phi^i, \phi_1, \phi_1'\right) = \sin \phi_1' e^{-ik\hat{\mathbf{r}} \cdot \mathbf{r}'} \mathbf{K}\left(\theta^i, \phi^i, \phi_1, \phi_1'\right) \tag{20}$$

Equation (19) represents the scattered fields resulting from the Fock current on the 3-D convex sphere scatterer.

After substituting Equation (14) or (16) into Equation (19), we obtain

$$\hat{\mathbf{r}} \cdot \mathbf{r} = P\left(\theta, \phi, \phi_1, \phi_1'\right) = R \sin \theta \sin \phi_1' \cos(\phi - \phi_1) + R \cos \theta \cos \phi_1' \tag{21}$$

Finally, $\mathbf{E}^{(s)}(\mathbf{r})$ in Equation (19) could be arrived at

$$\mathbf{E}^{(s)}(\mathbf{r}) = \underbrace{\frac{ikR^2 e^{ikr}}{4\pi r} \int_0^{2\pi} d\phi_1 \int_{\frac{\pi}{2}}^{\pi} d\phi_1' \mathbf{K}_1\left(\theta, \phi, \phi_1, \phi_1'\right)}_{\text{Contribution of the PO field and the NU-diffracted field in the lit region}}$$

$$\underbrace{+\frac{ikR^2 e^{ikr}}{4\pi r} \int_0^{2\pi} d\phi_1 \int_0^{\frac{\pi}{2}} d\phi_1' \mathbf{K}_2\left(\theta, \phi, \phi_1, \phi_1'\right)}_{\text{Contribution of the NU-diffracted field around the shadow boundary and in the deep shadow region}} \tag{22}$$

Here,

$$\mathbf{K}_1\left(\theta, \phi, \phi_1, \phi_1'\right) = \mathbf{V}_1(\theta, \phi, \phi_1, \phi_1') \sin \phi_1' e^{ik\left(\cos \phi_1' - P(\theta, \phi, \phi_1, \phi_1')\right)} G\left(\left(\frac{kR}{2}\right)^{\frac{1}{3}} \cos \phi_1'\right) \tag{23}$$

and $\mathbf{V}_1(\theta, \phi, \phi_1, \phi_1')$ takes the expression

$$\mathbf{V}_1(\theta, \phi, \phi_1, \phi_1') = \left(\sin \phi \cos \phi_1'\right) \hat{\phi} + \left(- \cos \theta \cos \phi \cos \phi_1' - \sin \theta \cos \phi_1 \sin \phi_1'\right) \hat{\theta} \tag{24}$$

Furthermore, $\mathbf{K}_2\left(\theta, \phi, \phi_1, \phi_1'\right)$ has the formulation

$$\mathbf{K}_2\left(\theta, \phi, \phi_1, \phi_1'\right) = \mathbf{V}_2(\theta, \phi, \phi_1, \phi_1') e^{-ikP(\theta, \phi, \phi_1, \phi_1')} e^{ikR\left|\frac{\pi}{2} - \phi_1'\right|} g\left(\left(\frac{kR}{2}\right)^{\frac{1}{3}} \left|\frac{\pi}{2} - \phi_1'\right|\right) \tag{25}$$

and $\mathbf{V}_2(\theta, \phi, \phi_1, \phi_1')$ is

$$\begin{aligned}
\mathbf{V}_2(\theta, \phi, \phi_1, \phi_1') &= \left(\cos \theta \sin \phi \sin \phi_1 \cos \phi_1' + \sin \theta \sin \phi_1' + \cos \theta \cos \phi \cos \phi_1 \cos \phi_1'\right) \hat{\theta} \\
&\quad + \cos \phi_1' \left(- \sin \phi \cos \phi_1 + \cos \phi \sin \phi_1\right) \hat{\phi}
\end{aligned} \tag{26}$$

At this point, the electric scattered fields from the Fock currents on the 3-D convex sphere by the ILDC technique are formulated, with the expression given in Equation (22). It contains two terms, the first term corresponds to the PO scattered field and the NU-diffracted field in the scatterer's lit region. The second term corresponds to the NU-diffracted field in the shadow region around the shadow boundary and the creeping wave fields in the deep shadow region. In the conventional ILDC technique [8, 12, 13], the contributions by the radiation integrals from the PO and NU currents are not separated. The PO contribution is expressed as a line integral along the shadow boundaries. Furthermore, the local ILDC coefficients are obtained by the asymptotic approximation of the line integrals from the NU currents.

5. THE EFFICIENT NUMERICAL CONTOUR DEFORMATION TECHNIQUE FOR CALCULATING THE FOCK CURRENT

In the lit and shadow regions of the considered convex scatterers, the Fock currents in Equation (14) or (16) have the highly oscillatory integrands, which are demonstrated in [20, 22, 23]. To efficiently evaluate the Fock currents, we propose the numerical contour deformation technique [20]. The idea is similar to our recent proposed numerical steepest descent path method (NSDP) for evaluating the PO scattered fields [18, 19].

For the observation points $\mathbf{r}$ lying in the shadow region with

$$\hat{\mathbf{k}}^i \cdot \hat{\mathbf{n}} > 0 \tag{27}$$

we propose the contour path Γ_s to calculate $g(x)$ [15]. Here, $\Gamma_s(t)$ is the integration path that starts from $-\infty$, and forms the angle $\arg(t) = \frac{2\pi}{3}$ with the $\mathrm{Re}(t)$ axis with $\mathrm{Re}(t) \leq 0$. While for the case $\mathrm{Re}(t) > 0$, $\Gamma_s(t)$ follows the path with $\arg(t) = 0$ [15]. However, for $\mathbf{r}$ lying in the lit region with

$$\hat{\mathbf{k}}^i \cdot \hat{\mathbf{n}} < 0 \tag{28}$$

we adopt the contour Γ_l in Figure 4. The saddle point S_* corresponds to the point where the derivative of the phase function with respect to the t variable in the integrand in Equation (13) equals to zero. To obtain the saddle point, the derivative of the Airy function is replaced with its asymptotics:

$$Ai'(t) \sim -\frac{t^{\frac{1}{4}}}{2\sqrt{\pi}} e^{-\frac{2}{3}t^{\frac{3}{2}}}, \quad |\arg(t)| < \pi \tag{29}$$

Here, the asymptotic formulations hold with the parameter $|t| \to \infty$ in Equation (29). Then, after substituting Equation (29) into Equation (13), the phase function in the kernel of $g(x)$ in Equation (13) is

$$p(x,t) = ixt - \frac{2}{3}t^{\frac{3}{2}} \tag{30}$$

On performing $\frac{\partial p(x,t)}{\partial t} = 0$, we obtain

$$ix - t^{1/2} = 0 \tag{31}$$

Hence, from Equation (31), $t = S_* = -x^2$ denotes the saddle point in Figure 4. With the case $\mathrm{Re}(t) \leq \mathrm{Re}(t_c)$, $\Gamma_l(t)$ is the integration path that starts from $-\infty$, and forms $\arg(t) = \frac{2\pi}{3}$ with the $\mathrm{Re}(t)$ axis. While with the case $\mathrm{Re}(t) > \mathrm{Re}(t_c)$, to avoid the saddle point S_* at the real $\mathrm{Re}(t)$ axis, $\Gamma_l(t)$ leaves the real axis with a small perturbation parameter $\varepsilon = 10^{-3}$ in our code. In detail, for the contour Γ_s, $t(s)$ is defined as $t(s) = e^{(i2\pi/3)}s$ for $s \in (-\infty, 0]$, and $t(s) = s$ for $s \in [0, \infty)$, respectively. For the contour Γ_l, $t(s)$ is defined as $t(s) = e^{(i2\pi/3)}s + t_c$ for $s \in (-\infty, 0]$, and $t(s) = s + t_c$ for $s \in [0, \infty)$, respectively. Here, in Figure 4, we adopt the contour with small perturbation parameter, which is similar as the Sommerfeld integration contour path of the Green's function.

5.1. Calculation of the Fock Function with the Gauss-Legendre Quadrature Rule

In the following numerical example, the observation point lies in the lit region of the convex scatterer, and the parameter x takes the value $x = -1.0074$. The observation point lies in the lit region of the convex cylinder with $\phi'_1 = 1.4304\pi$, as shown in Figure 3. The Gauss-Legendre quadrature rule with the number of $N = 20$ integration points was used. And the minimum and maximum integration step sizes are 0.1210 and 1.556, respectively. Here, the maximal and minimal step-sizes illustrate that the Gauss-Legendre nodes are not equidistant. By the integration of the integrated function in Equation (13), the contour path t is parameterized as $t = t(s)$, with s as the real parameter demonstrated in Figure 5. The Gauss-Legendre numerical integration scheme is

$$g(x) \approx -\frac{e^{i\pi/6}}{2\pi} \sum_{j=1}^{N} t'(s_j)w_j \frac{e^{ixt(s_j)}}{Ai'(t(s_j)e^{i2\pi/3})} \tag{32}$$

where s_j are the j-th integration points, w_j are the weights adopted in the Gauss-Legendre numerical scheme, $j = 1, 2, \ldots, N$. As is seen from Figure 5, both real and imaginary components of the integrated function function $g(x)$ become smooth ones after being defined along the complex contour deformation path Γ_l. Due to the fast decay behavior of the kernel of the Fock function, we could truncate the infinite contours to finite path intervals on the complex plane in the numerical integration process.

In detail, for evaluating the integrated function $g(x)$, we numerically truncate the integration contour $\Gamma_l(t)$ at the point t_*, where the amplitude of the kernel takes on the value less than a tolerance value v_*, i.e., $\mathrm{Kernel}(g(\Gamma_l(t_*))) \leq v_*$. Here, we set $v_* = 10^{-5}$ in our code. The reason why v_* is so small is that the integrand of $g(x)$ defined on $\Gamma_l(t_*)$ decays very fast after the contour deformation technique. In this manner, we truncate the infinite integration contour paths Γ_l and Γ_s to finite paths. Then, for finite integration intervals, we adopt the Gauss-Legendre quadrature rule to integrate $g(x)$ function with frequency independent workload and error controllable accuracy.

6. NUMERICAL EXAMPLES

In the following, we demonstrate the application of the ILDC technique to the 3-D convex scatterer. We consider the incident plane wave impinging from the positive z-direction, as shown in Figure 2(b). For the plane incident wave that is x-polarized, we study the scattered fields via the Fock current from the convex cylinder as shown in Figure 2(b).

In Figure 6, we consider the bistatic RCS values with cases $kR = 25$ and $kR = 30$, respectively. The sampling angle point at which the RCS is $M_j = j\pi/180$, $j = 0, 1, \ldots, 180$. The results of the scattered fields from the Fock current, the PO current and the Mie series methods are clearly demonstrated. As is shown in Figure 6, the scattered fields from the Fock current agree well with those generated by the Mie series method. Furthermore, one could observe that the scattered fields from the Fock current significantly improve the accuracy of the PO scattered fields. The reason is that the Fock current from the convex scatterer contains not only the PO current but also the NU-Fock current in the transition region and in the deep shadow region, which could agree well with the exact electric current from the convex scatterers. In Figure 6(b), compared to the RCS results via the MIE series method, the relative errors of the RCS values over all the sampling points by the Fock and PO methods are 0.088 and 0.3577, respectively. Hence, compared to the PO method, the accuracy of the scattered fields results could be significantly improved by the Fock current and the ILDC technique.
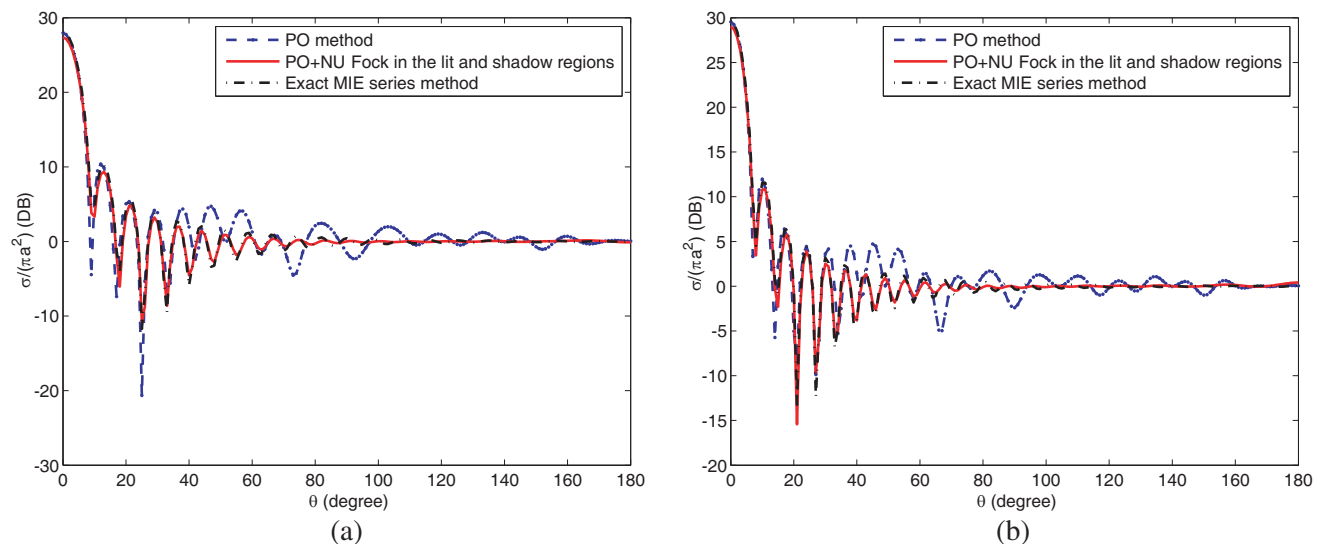
Figure 6. The far scattered fields from the 3-D conducting sphere are generated by the PO approximation current, the uniform Fock current in the scatterer's lit and shadow regions and the Mie series method, respectively. Here, the products of the wave frequencies and the radius of the sphere have the values (a) $kR = 25$, and (b) $kR = 30$, respectively.

To demonstrate the effect of the NU-Fock current in the shadow region, in Figure 7, we show the contributions of the creeping wave fields from the NU-Fock current in the shadow region. As is seen from Figure 7, the creeping wave fields become strong in the forward scattering direction, while they become weak in the backward direction. In summary, on invoking the ILDC technique for the 3-D convex scatterer, the scattered fields from the Fock currents gain high accuracy and could even agree well with the Mie series solution. The extension of the Fock currents to arbitrary 3-D convex scatterers will be considered in the future.
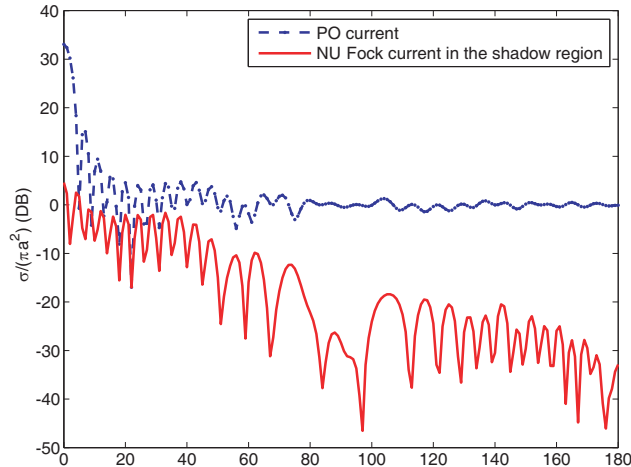
Figure 7. Comparison of the contributions of the PO scattered fields and the wave fields from the NU-Fock current in the shadow region of the sphere, with $kR = 45$.

7. CONCLUSIONS

The numerical contour deformation method is developed to efficiently evaluate the Fock currents. Furthermore, on invoking the ILDC technique, the high frequency scattered fields are elegantly formulated via the Fock currents. Numerical results for the 3-D convex PEC spheres demonstrate that the scattered fields via the Fock currents greatly enhance the accuracy from those produced by the PO currents.

REFERENCES

1. Song, J. M., C. C. Lu, and W. C. Chew, "Multilevel fast multipole algorithm for electromagnetic scattering by large complex objects," *IEEE Trans. Antennas Propag.*, Vol. 45, No. 10, 1488–1493, Oct. 1997.

2. Ling, H., R. C. Chou, and S. W. Lee, "Shooting and bouncing rays: calculating the RCS of an arbitrarily shaped cavity," *IEEE Trans. Antennas Propag.*, Vol. 37, No. 2, 194–205, 1989.

3. Tiberio, R., A. Toccafondi, A. Polemi, and S. Maci, "Incremental theory of diffraction: A new-improved formulation," *IEEE Trans. Antennas Propag.*, Vol. 52, No. 9, 2234–2243, Mar. 2004.

4. Rubinowicz, A., "Darstellung der sommerfeldschen beugungswelle in einer gestalt, die Beitrage der einzelnen elemente der beugende kante zur gesamten beugungswelle erkennen last," *Acta Phisica Polonica A*, Vol. 28, No. 6, 841–860, 1965.

5. Canta, S., D. Erricolo, and A. Toccafondi, "Incremental fringe formulation for a complex source point beam expansion," *IEEE Trans. Antennas Propag.*, Vol. 59, No. 5, 1553–1561, May 2011.

6. Mitzner, K. M., "Incremental length diffraction coefficients," Northrop Corp, Aircraft Div., Tech Rep. AFAL-TR-73-296, 1974.

7. Hansen, T. B. and R. A. Shore, "Incremental lenght diffraction coefficient for the shadow boundary of a general cylinder," Rome Laboratory, Air Force Material Command, Tech. Rep. RL-TR-97-151, 1997.

8. Breinbjerg, O., "Higher order equivalent edge currents for fringe wave radar scattering by perfectly conducting polygonal plates," *IEEE Trans. Antennas Propag.*, Vol. 40, No. 12, 1543–1554, Dec. 1992.

9. Fock, V. A., "The distributions of currents induced by a plane wave on the surface of a conductor," *J. Phys.*, Vol. 10, 130–136, 1946.

10. Shore, R. A. and A. D. Yaghjian, "Incremental diffraction coefficients for planar surfaces," *IEEE Trans. Antennas Propag.*, Vol. 36, No. 1, 55–70, Jan. 1988.

11. Michaeli, A., "Elimination of infinities in equivalent edge currents, Part I: Fringe current components," *IEEE Trans. Antennas Propag.*, Vol. 34, 912–918, Jul. 1986.

12. Michaeli, A., "Elimination of infinities in equivalent edge currents, Part II: Physical optics components," *IEEE Trans. Antennas Propag.*, Vol. 34, No. 8, 1986.

13. Hansen, T. B. and R. A. Shore, "Incremental length diffraction coefficients for the shadow boundary of a convex cylinder," *IEEE Trans. Antennas Propag.*, Vol. 46, No. 10, 1458–1466, Oct. 1998.

14. Yaghjian, A. D., R. A. Shore, and M. B. Woodworth, "Shadow boundary incremental length diffraction coefficients for perfectly conducting smooth, convex surfaces," *Radio Sci.*, Vol. 31, No. 6, 1681–1695, Dec. 1996.

15. Sandstrom, S. K., "A remark on the computation of Fock functions for negative arguments," *Int. J. Electron. Commun. (AEU)*, Vol. 62, No. 4, 324–326, Apr. 2008.

16. Wu, T. T., "High-frequency scattering," *Phys. Rev.*, Vol. 104, No. 5, 1201–1212, 1956.

17. Hönl, H., A. W. Maue, and K. Westpfahl, *Theory of Diffraction*, Springer, Berlin, 1961.

18. Wu, Y. M., L. J. Jiang, and W. C. Chew, "An efficient method for computing highly oscillatory physical optics integral," *Progress In Electromagnetics Research*, Vol. 127, 211–257, 2012.

19. Wu, Y. M., L. J. Jiang, W. E. I. Sha, and W. C. Chew, "The numerical steepest descent path method for calculating physical optics integrals on smooth conducting surfaces," *IEEE Trans. Antennas Propag.*, Vol. 61, No. 8, 4183–4193, Aug. 2013.

20. Wu, Y. M., L. J. Jiang, W. C. Chew, and Y. Q. Jin, "The contour deformation method for calculating the high ffrequency scattered field by the Fock current on the surface of the 3-D convex cylinder," *IEEE Trans. Antennas Propag.*, Vol. 63, No. 5, 2180–2190, May 2015.

21. Shore, R. A. and A. D. Yaghjian, "Shadow boundary incremental length diffraction coefficients applied to scattering from 3D bodies," *IEEE Trans. Antennas Propag.*, Vol. 49, No. 2, 200–210, Feb. 2001.

22. Wu, Y. M. and W. C. Chew, "The modern high frequency techniques for solving electromagnetic scattering problems," *Progress In Electromagnetics Research*, Vol. 156, 63–82, 2016.

23. Wu, Y. M. and S. J. Teng, "Frequency-independent approach to calculate physical optics radiations with the quadratic concave phase variations," *J. Comput. Phys.*, Vol. 324, 44–61, 2016.